

Open Experimental Measurements of Sub-6GHz Reconfigurable Intelligent Surfaces

Marco Rossanese , Placido Mursia , Andres Garcia-Saavedra , and Vincenzo Sciancalepore , NEC

Laboratories Europe GmbH, 69115, Heidelberg, Germany

Arash Asadi , TU Darmstadt, 64289, Darmstadt, Germany

Xavier Costa-Perez , i2CAT Foundation, 08034, Barcelona, Spain, NEC Laboratories Europe GmbH, 69115, Heidelberg, Germany, and ICREA, 17003, Barcelona, Spain

In this article, we present two datasets that we make publicly available for research.

The data is collected in a testbed comprised of a custom-made reconfigurable intelligent surface (RIS) prototype and two regular orthogonal frequency-division multiplexing (OFDM) transceivers within an anechoic chamber. First, we discuss the details of the testbed and equipment used, including insights about the design and implementation of our RIS prototype. We further present the methodology we employ to gather measurement samples, which consists of letting the RIS electronically steer the signal reflections from an OFDM transmitter toward a specific location. To this end, we evaluate a suitably designed configuration codebook and collect measurement samples of the received power with an OFDM receiver. Finally, we present the resulting datasets, their format, and examples of exploiting this data for research purposes.

Reconfigurable intelligent surfaces (RISs) are envisioned to become a key enabling technology for next-generation mobile systems, such as beyond 5G/6G. An RIS consists of an array of subwavelength unit cells that can alter the electromagnetic (EM) response of the impinging radio-frequency (RF) signals in a nearly passive way.

effectively create a virtual LoS, which guarantees favorable signal propagation conditions.² This can be achieved, for instance, by suitably designing the reconfigurable phase shift provided by each unit cell to receive wireless signals such that the reflected signals may interfere constructively toward the desired direction and destructively elsewhere.

BACKGROUND

Indeed, RISs can dynamically refocus the received EM waves toward desired directions in space by suitably configuring the scattering properties of each unit cell. This ability unlocks new possibilities and opens up a new paradigm of the wireless environment, which has been treated as an optimization constraint in conventional systems but can now be considered as a variable to be optimized, creating the so-called smart radio environment.¹ For example, when an obstacle hinders the line of sight (LoS) between the transmitter and the receiver, an RIS device strategically deployed can alleviate this problem via (passive) beamforming so as to

RIS Requirements

RISs are designed to be low-power, easy-to-manufacture, and low-cost devices. Hence, they are expected to satisfy the following requirements:

- › RISs should (re-)steer RF signals with minimal power loss.
- › RISs should not use active RF components.
- › RISs are expected to minimize the energy required to reconfigure their reflective cells.
- › RISs should be reconfigurable in real time.
- › RISs are expected to be amenable to low-cost production at scale.

Several RIS prototypes have recently been presented in the literature, each of which is designed in its unique way with its associated strengths and limitations

1089-7801 © 2024 IEEE

Digital Object Identifier 10.1109/MIC.2024.3376772

Date of publication 18 March 2024; date of current version 16 April 2024.

TABLE 1. Overview of datasets related to RIS.

Dataset	Frequency	Type	Description	Public
-	5.3 GHz	Measurements	Measurements collected in anechoic chamber with different numbers of RIS elements and with 3° intervals. RIS radiation patterns presented.	✓
[4]	5 GHz	Measurements	Measurements collected in anechoic chamber with 16×16 RIS with 5° intervals.	✓
[5]	Tunable	Generic	Generated using a custom path-loss prediction model.	X
[6]	Tunable	Generic	Generated based on the proposed RIS channel model.	X

while trying to fulfill these requirements. However, such designs are not always completely disclosed, making their replication and the associated results hard to realize. In addition, the data collected during the characterization of these prototypes is not shared within the community. Consequently, almost the totality of works tackling RIS challenges via machine learning (ML) algorithms rely on simulated data. Therefore, it is evident there is a lack of prototypes to test the new possible features and scenarios and a lack of data to elaborate more accurate models for this new communication paradigm.

Contributions

Motivated by these considerations, we decided to implement our RIS prototype, which fulfills the aforementioned design points, together with high-granularity beam steering, and to make publicly accessible the measurements collected during our tests in an anechoic chamber, in the hope it may be useful to foster the progress of the field.^a The design of our RIS prototype which is also briefly discussed in the “RIS Design” section has been thoroughly explained in Rossanese et al.³ This article extends our previous work by adding manifold contributions. First, we explain in detail how to set up an anechoic chamber for effective RIS measurements, and we share our experience to ease its replication. Second, we disclose a new dataset where we employed our unique absorption mode, and we explicate how the data collected in the anechoic chamber results is structured. Third, we present a series of ways of how these datasets can be employed, for instance, how to model a 3D radiation pattern for the RIS from 2D measurements, how a deep neural network (DNN) can

help to infer missing configurations, and how the absorption mode can be exploited for localization fingerprinting.

Related Works

This subsection gives a brief overview of existing RIS-related works, with a particular focus on datasets and some example of different prototype designs in the literature. Given the novel nature of this technology, publicly available datasets for RIS-based systems are rare today.

The only publicly accessible dataset derived from real measurements is delineated in Tewes et al.⁴ This dataset is constructed through the aggregation of S_{21} values, denoting the transmission gain from the input to the output port, conducted at a frequency of 5 GHz within an anechoic chamber by configuring a 16 × 16 RIS with 1-b phase shifter and using two distinct methodologies. It encompasses outcomes from both stationary configurations and the utilization of a rotating table, with adjustments made at intervals of 5°. Points of difference from our dataset include the absence of clearly delineated radiation patterns for the considered RIS, hindering its utility in other investigations; the provision of power values with a wider measurement interval; restriction to a single size of RIS elements; and a lack of accompanying use case illustrations for contextualization.

Other existing works consist of exploiting theoretical models of RIS-aided wireless communication systems. For instance, in Elshennawy,⁵ the authors generated a dataset using a custom path-loss prediction model. Similarly, a dataset based on a proposed RIS channel model is used in Alexandropoulos et al.⁶ In both cases, however, the respective datasets were not made public. The main aspects of these datasets are summarized in Table 1 for the reader’s convenience.

^aThe datasets and associated documentation are available at <https://github.com/marcantonio14/RIS-Power-Measurements-Dataset>.

Several RIS prototypes are present in the literature and they are built with different technologies and working at different frequencies.⁷ As in our case, an RF switch at the sub-6 GHz band is used in Trichopoulos et al.⁸ with a 1-b phase shifter. This solution is very efficient because it permits the achievement of high phase shifting granularity and low losses at limited costs; this is the main reason that drove us to choose this implementation. However, it must be said that at mmWave this technology is still immature, costly, and it can create undesired effects, such as beam squint, that must be properly addressed.

Another phase-shifting technology is PIN-diode, which is more suited for mmWave design, as shown for the prototypes working at 28 GHz presented in Li et al.⁹ and Dai et al.,¹⁰ while it can be used for sub-6 GHz solutions as well.¹¹ Although it is a versatile solution, it presents an important limitation on the achievable phase-shifting granularity. In fact, most of the prototypes employ just 1 b. Trying to increase this number would increase the costs together with the overall complexity since it requires the adoption of several PIN-diodes in a single unit cell.

Furthermore, there are varactor diodes, as employed for example in Pei et al.,¹² which can achieve high-granularity phase shifting at the cost of high power consumption. At the current stage, none of the suggested solutions can simultaneously achieve low costs, high efficiency, and low power consumption. Hence, the RIS designer needs to carefully choose the characteristics of the device based on the system constraints.

For high-frequency bands, new approaches are being investigated: for the mmWave case, in Cho et al.,¹³ an advanced unit cell structure working at 24.5 GHz is employed to permit the RIS to totally reflect or refract the incoming wave with the possibility to steer the output beam, while in Qian et al.,¹⁴ a reflecting surface can be rapidly created via 3D printing to steer the wave to the desired direction. It must be noted that this solution is not reconfigurable.

For the terahertz domain, instead, the research is still in its preliminary stages, and it is far from being considered mature. This is due to the high complexity of the components and architecture, as well as the extremely small dimensions of antennas. Currently, various tuning methods are being investigated, such as electronic approaches (CMOS transistors, Schottky diodes, high-electron-mobility transistors, and graphene), optical approaches (photoactive semiconductor materials), phase-change materials (vanadium dioxide, chalcogenides, and liquid crystals), and microelectromechanical systems.¹⁵

RIS DESIGN

The datasets that we present in this article have been generated by experimenting with a custom-made RIS prototype, whose design was presented in detail in Rossanese et al.³ To provide some context, we summarize next the most important aspect of this device.

Our RIS prototype consists of 100 patch antennas in a 10×10 grid of *unit cells* (each with one antenna), implemented with printed circuit board (PCB) technology on a board with a thickness of 0.6 mm. The antennas are separated by a distance equal to $\lambda/2$, both horizontally and vertically, with λ being the wavelength of the supported carrier signals. The operating frequency of the RIS is 5.3 GHz, with a bandwidth equal to 100 MHz. The final RIS prototype printout is depicted on the right-hand side of Figure 1.

This prototype achieves passive beamforming via phase shifting of the impinging RF signal with 3-b granularity. This is implemented with suitably designed delay lines (microstrip lines in PCB): each patch antenna is connected to an RF-switch, a device that redirects an input RF signal toward one output port, while isolating the others, depending on a set configuration. The RF-switch possesses eight outputs, each of which is connected to an open-ended transmission line whose length determines the applied phase shift. Once the signal has traveled through the selected delay line, it is retransmitted by the antenna. By applying the correct configuration to each RF switch it is possible to perform passive beamforming.

A microcontroller is in charge of configuring the RIS with the desired configuration in each unit cell. Notably, our design allows controlling each unit cell by means of a grid of configuration buses. This approach avoids the direct connection of each component to the microcontroller. Indeed, with this scheme, the total number of connections to the microcontroller is equal to the sum of rows and columns (i.e., $10 + 10$ in our case), as opposed to one connection per unit cell (i.e., 100), thus providing a good level of scalability. A conceptual schematic of the RIS is depicted in Figure 2. The average time to configure a single unit cell is 0.35 ms, and its power consumption is 62 mW. We would like to remark that the number of unit cells has a limited impact on the power consumption since they are comprised of elementary components. On the other hand, the microcontroller unit (MCU) plays a major role here because it is set to best performance mode. As part of our future work, we plan to modify the MCU to enable deep sleep mode, which will conserve power when the RIS is idle. According to the datasheet,



FIGURE 1. RIS board prototype (amplified in the right-hand side of the figure) in an anechoic chamber along with an OFDM transmitter (TX) and an OFDM receiver (RX) used to obtain the measurements provided in the dataset presented in this article.³

the power consumption in sleep mode can be reduced to approximately $1\text{ }\mu\text{W}$.

The RIS is designed to be a modular device. This means that multiple RIS boards can be connected together, thus creating a larger RIS, while still respecting the $\lambda/2$ inter-element distance even between cross-board elements.

Finally, a peculiar characteristic of our RIS prototype is the *absorption mode*, i.e., a state in which each unit cell redirects the incoming signal through one of the eight RF switch outputs to a $50\text{ }\Omega$ resistor that will dissipate the incoming signal. That is, the unit cell configured with this mode will not reflect the received signal. This feature unlocks novel applications such as

virtual reshaping or rescaling of the RIS array shape in real time.

TESTBED SETUP AND IMPLEMENTATION

In the following, we first present our experimental setup by describing the physical scenario, the lab equipment employed, and the measurement methodology that led to the provided datasets.

Our measurements were performed in a 5×8 m anechoic chamber: a controlled environment that is isolated from external EM interference. In such a scenario, the EM waves generated by a transmitter within

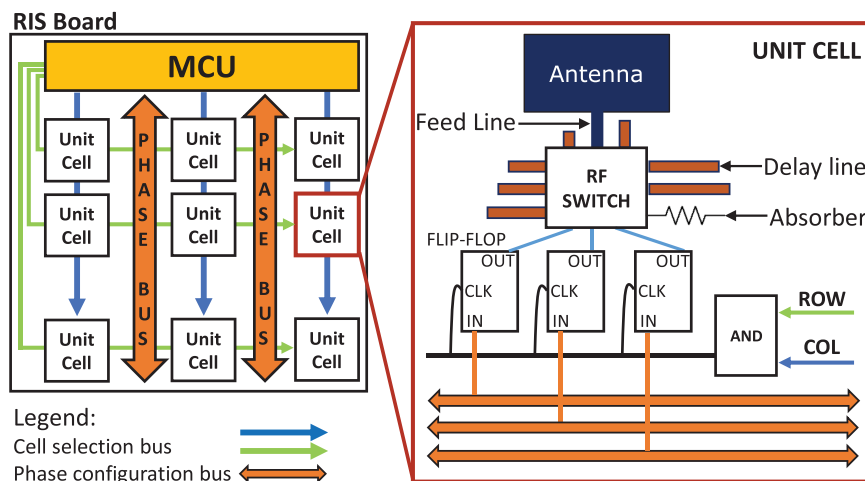


FIGURE 2. RIS board schematic.³

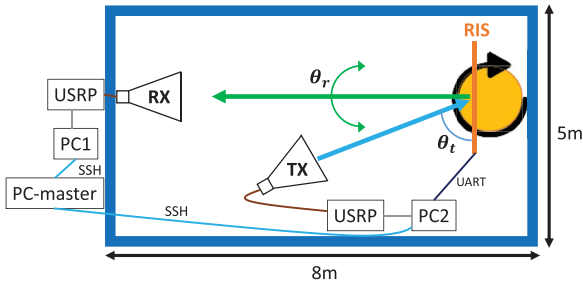


FIGURE 3. Anechoic chamber testbed bird's-eye view.³ USRP: universal software radio peripheral.

the chamber are absorbed by *RF absorbers*, i.e., lossy material shaped to allow for incoming EM waves to penetrate with minimal reflections, which are placed on the walls, ceiling, and on the floor. Hence, the channel between the transmitter and the receiver is characterized by the direct LoS link only. Note that, for our purposes, it is essential to maintain a LoS channel, as it may be hard to distinguish between the RIS-reflected contribution and any other *multipath* scattered signal components. In practice, it is not possible to block completely all other undesired paths; nevertheless, the anechoic chamber is designed to produce a reflection-free area, called *quiet zone*, wherein the devices to be tested are placed.

In our setup, we place a turntable in the quiet zone, as shown in Figure 3, which can be remotely controlled by a computer, dubbed as *PC-master*, in a control room adjacent to the anechoic chamber. This PC has the crucial role of coordinating the transmitting antenna (TX), the receiving antenna (RX), the rotation of the table, and the RIS configuration. Indeed, it instructs two additional laptops, namely *PC1* and *PC2*, which are placed outside and inside the chamber, respectively, using SSH communication protocol. *PC1* is used to collect measurements from the RX. Conversely, *PC2*, which is connected to the RIS, receives instructions from the master PC via a Python script that selects the desired RIS configuration. This communication is realized via universal asynchronous receiver-transmitter communication protocol. *PC2* is also connected to the TX, and it thus forwards the necessary transmission parameters received from the master PC. Finally, the master PC is also directly connected to the turntable motor.

The RIS is installed on a pole vertically mounted onto the turntable. On the same turntable, another pole is horizontally mounted and used as a base for the TX. This setup allows us to fix the angle of arrival (AoA) of signals sent from the TX to the RIS and keep it

constant for every rotation of the turntable. The TX is located at $d_{RIS-TX} = 1.1$ m from the first top-left element of the RIS, with an azimuth angle of 90° , and an elevation angle of -33° . The RX is deployed at an azimuth angle of 90° and an elevation angle of -3° in front of the RIS, and it is placed at 6.3 m away from the top-left antenna element.

All such relative distance and angle measurements were collected with the GLM50C laser measurer and are summarized in Figure 2. Given the RIS diagonal $D = 0.43$ m and its operating frequency of 5.3 GHz, it is hard to guarantee that the distance RIS-TX is larger than the far-field threshold, which is equal to $D = 0.43$ m.¹⁶ Nevertheless, our choice of d_{RIS-TX} is larger than the reactive near-field threshold, which is $0.62\sqrt{\frac{D^3}{\lambda}} = 0.73$ m,¹⁶ and thus sufficiently large for our purposes.

The TX and RX are implemented via two small double-ridged horn antennas, namely TBMA4, with a frequency range of 1–8 GHz, that exhibit a gain of 13.5 dBi and a voltage standing wave ratio of ~ 1 at our operating frequency. Furthermore, its nominal impedance is $50\ \Omega$.

The signal feeding the TX is generated by a dual-channel transceiver universal software radio peripheral (USRP) model B210, offering continuous RF coverage in the range of 70 MHz to 6 GHz. On the RX side, another B210 USRP is used to sample and decode the incoming signal. The USRPs run the srsRAN software, i.e., an open-source software-defined radio 4 G/5G software suite from software radio systems (SRS), which can process orthogonal frequency-division multiplexing (OFDM) LTE-like RF signals. More specifically, the TX-side USRP is used to generate a continuous stream of OFDM quaternary phase-shift keying-modulated symbols with 5 MHz of bandwidth, a transmit power of -30 dBm per subcarrier, and numerology that meets the 3GPP LTE requirements. Whereas the RX-side USRP measures the reference signal received power (RSRP), averaged across the signal bandwidth. In particular, the srsRAN version at the RX side was modified to conveniently dump the measured RSRP values into a file that will be later parsed and analyzed.

Considering the quasi-static nature of the channel in the anechoic chamber, a small number of RSRP samples should be enough to obtain meaningful statistics. However, random fluctuations in RSRP are possible due to several factors, such as imperfect chamber isolation, intrinsic receiver noise, and so on. Increasing the number of samples per measurement may help alleviate this problem, but dramatically increases the experimentation time. In order to strike a balance between speed and reliability of the measurements, we performed an initial experiment by pointing the

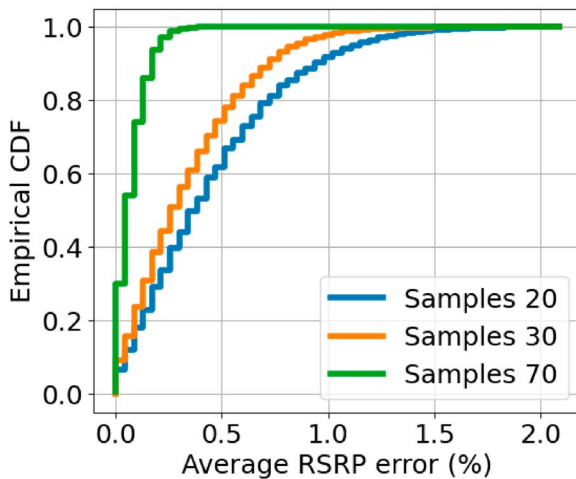


FIGURE 4. Empirical CDF for the RSRP averaged over different number of samples as compared to the ground truth.

turntable toward the RX and setting the RIS to sweep over a codebook of 3721 predefined RIS configurations. We collected a total of 80 RSRP samples for every RIS configuration, with a rate of 4 ms. Given the LTE coherence time of 1 ms and the slow-changing channel in the anechoic chamber, we selected a sampling rate that is large enough to avoid inter-symbol interference. By assuming that RSRP averaged over the 80 samples represents the *ground truth*, we then analyzed the average RSRP over a variable (and lower) number of samples, as depicted in Figure 4. Here, we show the empirical cumulative distribution function (CDF) for the difference between the average RSRP over a variable number of collected samples versus the value averaged over 80 samples. Based on these results, it is possible to see that the average RSRP error is smaller than 1% for the 90% of cases when 20 samples only are taken; similarly, the error drops to 0.7% when the amount of samples is 30. Therefore, we empirically chose 30 samples, in order to keep the measured RSRP error on average below 1%, and simultaneously reduce the total time of experimentation.

We performed our tests using two predefined RIS configuration codebooks, both of which are designed by assuming a geometrical *phase-shift* channel model, whereby the received signal from the RIS to a specific location in space identified by the azimuth and elevation angles (θ_r, ϕ_r) is given as⁷

$$y = \mathbf{h}(\theta_r, \phi_r)^H \Phi \mathbf{g}(\theta_t, \phi_t) + n \in \mathbb{C}$$

where $\mathbf{h}(\theta_r, \phi_r) \in \mathbb{C}^{N \times 1}$ is the channel from the (N -element) RIS to the RX, $\Phi = \text{diag}(e^{j\phi_1}, \dots, e^{j\phi_N}) \in \mathbb{C}^{N \times N}$ is the diagonal matrix containing the RIS phase

shifts, $\mathbf{g}(\theta_t, \phi_t) \in \mathbb{C}^{N \times 1}$ is the channel from the TX, located at azimuth and elevation angles (θ_t, ϕ_t) , to the RIS, and n is the noise term. Since our experiments are performed within an anechoic chamber, we adopt a purely LoS model for the channel vectors as

$$\begin{aligned} \mathbf{h}(\theta_r, \phi_r) &= \mathbf{a}_x(\theta_r) \otimes \mathbf{a}_y(\phi_r) \\ &= [1, e^{j2\pi\delta \cos(\theta_r)}, \dots, e^{j2\pi\delta(N_x-1)\cos(\theta_r)}] \\ &\quad \otimes [1, e^{j2\pi\delta \sin(\phi_r)}, \dots, e^{j2\pi\delta(N_y-1)\sin(\phi_r)}] \end{aligned}$$

with $\delta = 0.5$ the ratio between the interelement spacing and the signal wavelength, N_x and N_y the number of antennas on the rows and columns of the RIS, respectively, and \otimes the Kronecker product. Note that $\mathbf{g}(\theta_t, \phi_t)$ is defined similarly.

In the first case, each configuration is created to point the main beam of the RIS reflection pattern toward a precise and unique direction in space. In particular, the main beam is scanned on the azimuth in the range of $[-90^\circ, 90^\circ]$ and $[-45^\circ, 45^\circ]$ on the azimuth and elevation, respectively, with a step of 3° in both cases. Hence, the codebook contains a total of 1891 different configurations.

The turntable is configured to move in the range $[-90^\circ, 90^\circ]$ with a step of 3° along the azimuth plane. As stated above, the angle between the surface of the RIS and the RX along the azimuth plane is denoted by θ_r . For each value of θ_r , which corresponds to an equal rotation angle of the table, we let the RIS scan through all the configurations in the codebook, and we collect the RSRP power measurements at PC1, as described above. The total time for the complete characterization is 9 h. Given the high directionality expected in the reflections generated by the RIS (passive beamforming), we expect the RSRP to be maximum when the main beam is pointing toward the RX and very small elsewhere. However, besides verifying the directionality of our prototype, we are interested in assessing the impact of side lobes.

The aforementioned measurement procedure is replicated for two different TX locations, defined with θ_t , equal to 20° and 90° , respectively, where the latter corresponds to having the TX exactly in line with the RIS.

In the second codebook, the absorption mode feature is used to create subarrays of $N \times N$ active elements located on the top left of the RIS, leaving all remaining antenna elements turned off. In this scenario, the table is not rotating, and the receiver, transmitter, and RIS are all aligned. The main beam is scanned as in the previous case, accounting for fewer active antenna elements.

Finally, in order to properly scale the collected RSRP measurements, we evaluated the noise floor in

TABLE 2. Snippet of the two datasets. On the left, the dataset for the full RIS array and rotating table (*beampattern dataset*); the name of the file indicates the value of θ_t . On the right, the dataset for fixed table position and different numbers of active RIS antenna elements (*absorption mode dataset*).

	Table Rotation: θ_r			
Beam: $(\theta_n; \Phi_n)$	-90°	90°
$(-90^\circ; -45^\circ)$	Power (dBm)	Power (dBm)
$(-90^\circ; -42^\circ)$	Power (dBm)	Power (dBm)
.
.

	Active elements N			
Beam: $(\theta_n; \Phi_n)$	4	16	64	100
$(-90^\circ; -45^\circ)$	Power (dBm)	Power (dBm)
$(-90^\circ; -42^\circ)$	Power (dBm)	Power (dBm)
.
.

the anechoic chamber at a level of -90 dbm by collecting the RSRP when the RIS is plugged off.

DATASETS AND THEIR USAGE

After the required data postprocessing (e.g., parsing the RSRP dump files), we consolidated the measurements we gathered in the anechoic chamber in two datasets that we made publicly available.

In the first dataset, we used the full RIS array while rotating the turning table (dubbed as *beampattern dataset*); in the second one, the table is fixed with RX, TX, and RIS aligned, while we vary the number of active antenna elements (namely, *absorption mode dataset*).

We believe these datasets can be very useful to the community. Hence, in the following, we describe them in detail and present different use cases that exemplify how this data can be exploited for research.

Beampattern Dataset

In the former case, for each RIS configuration and rotation angle of the table, the 30 collected samples are averaged and stored in the associated cell of a matrix: each row corresponds to the main beam direction, expressed with the couple of angles (θ_n, ϕ_n) , where θ_n and ϕ_n are the azimuth and the elevation, respectively; each column is associated with a different value of θ_r , which indicates the rotation angle of the table with respect to the RX. This is illustrated in **Table 2**. Furthermore, to ease manipulation, we split this dataset into two different files for the two values of θ_t , which are reflected in the file name.

Since the channel in the anechoic chamber is quasi-static, we deduced that the main factor adding noise to our RSRP measurements was related to the imperfections of the electronic components used in the RIS or the elements comprising the chamber itself. To smoothen our data, we applied a Savitzky–Golay filter, which is a common technique for smoothing data and calculations based on noisy data. Given a measured signal of N points and a filter window of width w , i.e., a subset of N , the Savitzky–Golay filter calculates a polynomial fit of order o in every window as it is moved across the signal points.¹⁷ A good choice for our case, in which $N = 61$, was using $w = 7$ and $o = 4$.

Each row in the dataset represents the RIS reflection pattern, given a beamforming configuration, i.e., main beam orientation in space, in the range $[-90^\circ, 90^\circ]$ on the azimuth plane. Given the elevation angles between the TX and the RIS (33°), and between the RIS and the RX (-3°) were kept fixed during the experiments, it is possible to calculate the direction of the main beam in elevation that maximizes the RSRP: the difference between these values yields -30° , which indicates that the RIS is “virtually” generating a main beam pointing to the ceiling. This compensates for the displacement between TX and RX on the elevation plane.

In **Figure 5**, we visualize with blue lines the rows in the dataset corresponding to azimuth angles of $\theta_n = -18^\circ$, $\theta_n = 0^\circ$, $\theta_n = 30^\circ$, and $\theta_n = 60^\circ$ along the direction that maximizes the RSRP in the elevation, i.e., $\phi_n = -30^\circ$. The measured reflection patterns (in blue) are in accordance with what we expected for an array

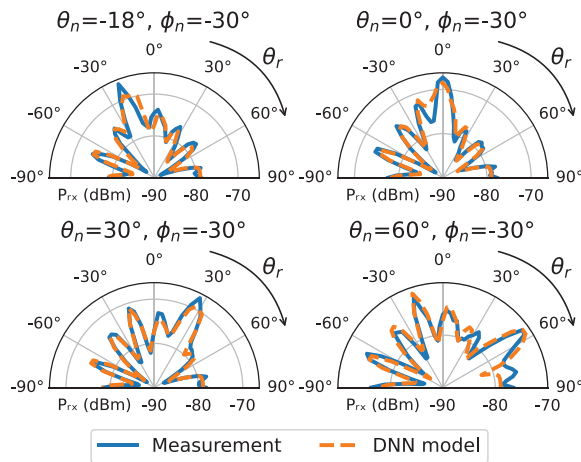


FIGURE 5. Power received at a fixed receiver for different values of the main beam direction in the azimuth and elevation of the RIS, represented by θ_n and ϕ_n , respectively. The measured data is shown in blue color, while the orange lines represent the prediction via DNN.

of patch antennas; furthermore, they demonstrate the beam-steering capabilities of our RIS prototype. By using this data, it is possible to retrieve simple, yet fundamental, parameters related to the RIS, such as the half power beam width (HPBW) or the radar cross section.

This data is amenable to ML models. To demonstrate this, we trained a simple DNN to learn the radiation pattern of our RIS prototype for each configuration in the codebook. In particular, we generated a DNN, consisting of three layers of 16 neurons each. The chosen loss function is the mean-squared error (MSE), while Adam was used as the optimizer. We reorganized the dataset in order to feed it to the DNN by arranging the values of θ_n , ϕ_n , θ_r , and the measured RSRP as columns. This new array is then split into two subsets for training and validation of the DNN. The network is trained for 750 epochs and a batch size set to 100 rows of the dataset.

This simple model approximates our dataset very accurately, with a normalized MSE equal to 0.01% for the training set and 0.03% for the validation set. To visualize this, Figure 5 depicts with orange lines some example values in comparison to the ground truth (in blue): the DNN can accurately predict the location and magnitude of the main beams and associated side lobes, as well as the null points. This model can also be used to infer the missing configurations due to the chosen 3° step.

Another useful application of the dataset is the reconstruction of a 3D RIS reflection pattern.

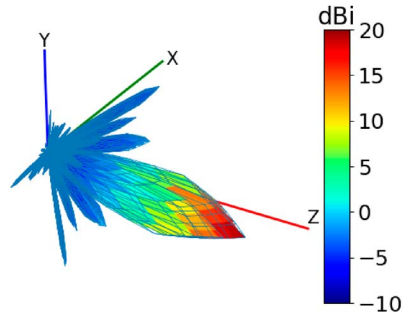


FIGURE 6. 3D reconstruction of the RIS radiation pattern using the HPI algorithm and the provided dataset.

Generally, to accomplish this task, it is necessary to possess information on two orthogonal planes, but in our case, we can rely only on the azimuth plane. However, given the squared geometry of our prototype array of patch antennas, it is possible to exploit the symmetry between azimuth and elevation planes for the radiation pattern. By exploiting the interpolation algorithm called horizontal projection interpolation (HPI), which is suited for the radiation shows an electrical tilt, i.e., when the main beam is not exactly perpendicular to the radiating device.¹⁸ The obtained result is shown in Figure 6.

Absorption Mode Dataset

Regarding the second dataset, we fixed the rotating table at $\theta_r = 0$ and exploited the absorption mode

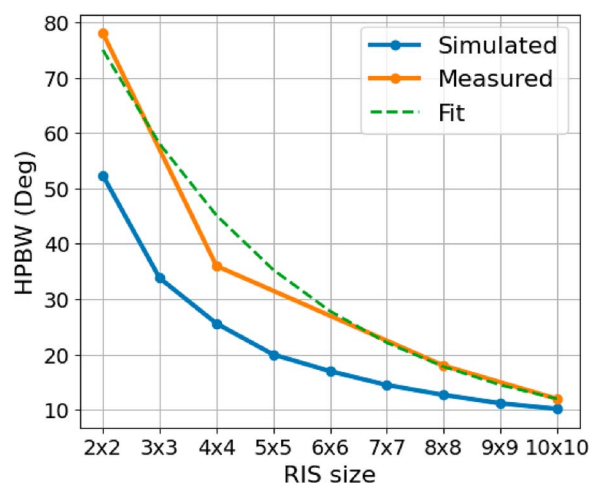


FIGURE 7. HPBW for different RIS sizes collected in the anechoic chamber (orange color), simulated via CST (blue color), and an exponential fit to the measured data (green color).

feature of our RIS prototype, thereby reshaping the number of active antenna elements to 4, 16, 64, and 100. The main purpose of this test is to explore the relationship between the beamforming gain and the number of antenna elements.

In this regard, we propose a model for half power beamwidth (HPBW) estimation as a function of the number of (active) RIS elements. Indeed, it is well known that the theoretical computation of the HPBW for a planar array is a difficult task.¹⁶ However, as shown in orange color in Figure 7, it appears that the HPBW measured from our RIS prototype follows an exponential trend. To confirm this intuition, we used the HPBW of several RIS structures computed in CST Studio as a benchmark, which is shown with a blue color. Both the measured and synthetic data exhibit a similar trend, with a gap between the two curves, which depends on several nonidealities such as, e.g., imperfect RIS hardware, and measurement uncertainty. Moreover, in green color, we show an exponential fit of the form $a \cdot \exp(b \cdot x) + c$ to the measured data, with x being the RIS size and parameters $a = 70.96$, $b = 0.27$, and $c = 3.99$ calculated with the nonlinear least squares method.

Our RIS prototype is modular and can be easily scaled to structures larger than 10×10 . This allows us to estimate the HPBW for larger RIS structures, which is important for localization. By reading the beampattern dataset in Table 2 by columns, we can gain insights into the performance of RIS-based localization techniques. Each column represents a different user position from the RIS point of view. To estimate the AoA/departure from/to the user, simply select the main beam direction corresponding to the maximum received power for every rotation angle of the table. The selected main beam direction can then be mapped to the corresponding RIS configuration codebook entry.

CONCLUSION

RISs represent a promising technology that will play a major role in future mobile systems designs. In this article, we have presented a dataset collected in an empirical setting comprised of an OFDM transmitter, an OFDM receiver, and a custom-built fully configurable sub-6 GHz RIS prototype within an anechoic chamber. We have introduced the design and corresponding features of the RIS by presenting the methodology employed to gather empirical data in the system for a wide set of configurations from a high-resolution codebook, and we have provided examples to illustrate the usefulness of our dataset. We hope that this publicly available dataset collecting measurements in an RIS-

aided wireless communication system will help in achieving a wide deployment of sub-6 GHz RISs in the future.

ACKNOWLEDGMENTS

The research leading to these results was supported in part by SNS JU Project 6G-DISAC (Grant 101139130) and BeGREEN (Grant 101097083).

REFERENCES

- M. Di Renzo et al., "Smart radio environments empowered by reconfigurable intelligent surfaces: How it works, state of research, and the road ahead," *IEEE J. Sel. Areas Commun.*, vol. 38, no. 11, pp. 2450–2525, Nov. 2020, doi: [10.1109/JSAC.2020.3007211](https://doi.org/10.1109/JSAC.2020.3007211).
- P. Mursia, V. Sciancalepore, A. Garcia-Saavedra, L. Cottatellucci, X. Costa-Perez, and D. Gesbert, "RISMA: Reconfigurable intelligent surfaces enabling beamforming for IoT massive access," *IEEE J. Sel. Areas Commun.*, vol. 39, no. 4, pp. 1072–1085, Apr. 2021, doi: [10.1109/JSAC.2020.3018829](https://doi.org/10.1109/JSAC.2020.3018829).
- M. Rossanese, P. Mursia, A. Garcia-Saavedra, V. Sciancalepore, A. Asadi, and X. Costa-Perez, "Designing, building, and characterizing RF switch-based reconfigurable intelligent surfaces," in Proc. 16th ACM Workshop Wireless Netw. Testbeds, Exp. Eval. Characterization, 2022, pp. 69–76, doi: [10.1145/3556564.3558236](https://doi.org/10.1145/3556564.3558236).
- S. Tewes, M. Heinrichs, K. Weinberger, R. Kronberger, and A. Sezgin, "A comprehensive dataset of RIS-based channel measurements in the 5GHz band," in Proc. IEEE 97th Veh. Technol. Conf. (VTC2023-Spring), 2023, pp. 1–5, doi: [10.1109/VTC2023-Spring57618.2023.10200973](https://doi.org/10.1109/VTC2023-Spring57618.2023.10200973).
- W. Elshennawy, "Large intelligent surface-assisted wireless communication and path loss prediction model based on electromagnetics and machine learning algorithms," *Prog. Electromagn. Res. C*, vol. 119, pp. 65–79, Mar. 2022, doi: [10.2528/PIERC22013002](https://doi.org/10.2528/PIERC22013002).
- G. C. Alexandropoulos, S. Samarakoon, M. Bennis, and M. Debbah, "Phase configuration learning in wireless networks with multiple reconfigurable intelligent surfaces," in Proc. IEEE Globecom Workshops (GC Wkshps), Piscataway, NJ, USA: IEEE, 2020, pp. 1–6, doi: [10.1109/GC_Wkshps50303.2020.9367575](https://doi.org/10.1109/GC_Wkshps50303.2020.9367575).
- J. Huang et al., "Reconfigurable intelligent surfaces: Channel characterization and modeling," *Proc. IEEE*, vol. 110, no. 9, pp. 1290–1311, Sep. 2022, doi: [10.1109/JPROC.2022.3186087](https://doi.org/10.1109/JPROC.2022.3186087).
- G. C. Trichopoulos et al., "Design and evaluation of reconfigurable intelligent surfaces in real-world environment," *IEEE Open J. Commun. Soc.*, vol. 3, pp. 462–474, 2022, doi: [10.1109/OJCOMS.2022.3158310](https://doi.org/10.1109/OJCOMS.2022.3158310).

9. Y. Li, Y. Ren, F. Yang, S. Xu, and J. Zhang, "A novel 28 GHz phased array antenna for 5G mobile communications," *ZTE Commun.*, vol. 18, no. 3, pp. 20–25, 2020, doi: [10.12142/ZTECOM.202003004](https://doi.org/10.12142/ZTECOM.202003004).
10. L. Dai et al., "Reconfigurable intelligent surface-based wireless communications: Antenna design, prototyping, and experimental results," *IEEE Access*, vol. 8, pp. 45,913–45,923, 2020, doi: [10.1109/ACCESS.2020.2977772](https://doi.org/10.1109/ACCESS.2020.2977772).
11. A. Araghi et al., "Reconfigurable intelligent surface (RIS) in the sub-6 GHz band: Design, implementation, and real-world demonstration," *IEEE Access*, vol. 10, pp. 2646–2655, 2022, doi: [10.1109/ACCESS.2022.3140278](https://doi.org/10.1109/ACCESS.2022.3140278).
12. X. Pei et al., "RIS-aided wireless communications: Prototyping, adaptive beamforming, and indoor/outdoor field trials," *IEEE Trans. Commun.*, vol. 69, no. 12, pp. 8627–8640, Dec. 2021, doi: [10.1109/TCOMM.2021.3116151](https://doi.org/10.1109/TCOMM.2021.3116151).
13. K. W. Cho, M. H. Mazaheri, J. Gummesson, O. Abari, and K. Jamieson, "mmWall: A steerable, transreflective metamaterial surface for NextG mmWave networks," in *Proc. 20th USENIX Symp. Netw. Syst. Des. Implementation (NSDI)*, 2023, pp. 1647–1665.
14. K. Qian, L. Yao, X. Zhang, and T. N. Ng, "MilliMirror: 3D printed reflecting surface for millimeter-wave coverage expansion," in *Proc. 28th Annu. Int. Conf. Mobile Comput. Netw.*, 2022, pp. 15–28, doi: [10.1145/3495243.3517024](https://doi.org/10.1145/3495243.3517024).
15. F. Yang, P. Pitchappa, and N. Wang, "Terahertz reconfigurable intelligent surfaces (RISs) for 6G communication links," *Micromachines*, vol. 13, no. 2, 2022, Art. no. 285, doi: [10.3390/mi13020285](https://doi.org/10.3390/mi13020285).
16. C. A. Balanis, *Antenna Theory: Analysis and Design*. Hoboken, NJ, USA: Wiley, 2016.
17. N. B. Gallagher, "Savitzky-Golay smoothing and differentiation filter," Eigenvector Research Incorporated, Manson, WA, USA, 2020. [Online]. Available: <https://eigenvector.com/wp-content/uploads/2020/01/SavitzkyGolay.pdf>
18. "Horizontal projection interpolation (HPI) algorithm." Altair Feko. Accessed: Sep. 2, 2022. [Online]. Available: https://2021.help.altair.com/2021/winprop/topics/winprop/user_guide/aman/introduction/horizontal_projection_interpolation_winprop.htm

MARCO ROSSANESE is a researcher at NEC Laboratories Europe GmbH, 69115, Heidelberg, Germany. His research interests include reconfigurable intelligent surfaces. Rossanese

received his M.Sc. degree in telecommunication engineering from Università degli Studi di Padova. Contact him at marco.rossanese@neclab.eu.

PLACIDO MURSIA is a research scientist in the 6GN Group, NEC Laboratories Europe GmbH, 69115, Heidelberg, Germany. His research interests include convex optimization, signal processing, and wireless communication. Mursia received his Ph.D. degree from Sorbonne Université of Paris. He is a Member of IEEE. Contact him at placido.mursia@neclab.eu.

ANDRES GARCIA-SAAVEDRA is a principal researcher at NEC Laboratories Europe GmbH, 69115, Heidelberg, Germany. His research interests include the application of fundamental mathematics to real-life wireless communication systems. Garcia-Saavedra received his Ph.D. degree from Universidad Carlos III de Madrid. Contact him at andres.garcia.saavedra@gmail.com.

VINCENZO SCIANCALEPORE is a principal researcher at NEC Laboratories Europe GmbH, 69115, Heidelberg, Germany. His research interests include reconfigurable intelligent surfaces. Sciancalepore received his double Ph.D. degrees in telematics engineering from Universidad Carlos III de Madrid. He is a Senior Member of IEEE. Contact him at vincenzo.sciancalepore@neclab.eu.

ARASH ASADI is a research group leader in the Wireless Communication and Sensing Lab, TU Darmstadt, 64289, Darmstadt, Germany. His research interests include wireless communication and sensing for beyond-5G/6G networks. Asadi received his Ph.D. degree in telematics engineering from Universidad Carlos III de Madrid. Contact him at aasadi@wise.tu-darmstadt.de.

XAVIER COSTA-PEREZ is a scientific director at i2CAT Foundation, 08034, Barcelona, Spain, head of 5G/6G R&D at NEC Laboratories Europe GmbH, 69115, Heidelberg, Germany, and a research professor at ICREA, 17003, Barcelona, Spain. His research interests include 6G, AI, ISAC, and RIS. Costa-Perez received his Ph.D. degree in telecommunications from the Polytechnic University of Catalonia. He is a Senior Member of IEEE. Contact him at xavier.costa@neclab.eu.